The Effect of TNT Mass and Standoff Distance on the Response of Fully Clamped Circular Aluminum Plates to Confined Air-Blast Loading

Kelly S. Carney [a], Paul DuBois [a], Stanisław Cudziło [b], Glenn A. Jorgensen [c], Wieslaw K. Binienda [d,*]

[a] *Forming Simulation Technology, LLC, 45529 Pebble Beach Ct., Detroit, MI 48168, United States*
[b] *Military University of Technology, ul. gen. Sylwestra Kaliskiego 2, 00-908 Warszawa 49, Warsaw, Poland*
[c] *ROBUST ApS, Sdr. Asmindrup, 4390 Vipperød, Denmark*
[d] *The University of Akron, Dept. of Civil Engineering, Akron, OH 44325-3905*

A B S T R A C T

An experimental and numerical investigation was conducted to examine the response of fully clamped, 2-mm-thick, 255-mm-diameter, circular plates of Aluminum 2024-T3 to confined air-blast loading. The plates were subjected to pressure loading generated by detonating varying charge masses of trinitrotoluene (TNT) at several axial positions in the chamber. In the first set of experiments, the charge mass was varied from 14 g to 50 g and the charge was located at the center of the chamber. In the second set, all charges were 15 g in mass, but they were detonated at different standoff distances. The experimental parameters for the explosive charge mass and the standoff distance needed to produce initial cracks in the aluminum plates as well as the permanent deflections of the uncracked plates were determined. The tests were simulated using the Arbitrary Lagrangian-Eulerian capability in the LS-DYNA commercial finite element program. The numerical simulations generally produced a good match both to the onset of fracture and the permanent displacements in the test plates. The presence of afterburn was demonstrated in a separate test where no oxygen was present, and a better match of the permanent displacements produced by the smallest charges was obtained when afterburn was included in the simulation. The finite element mesh, analysis approach, and blast modeling methodology can be used as a design or evaluation tool for the analysis of potential blast events in full-scale aircraft.

1. Introduction

Explosives have been used in a number of terrorist attacks on aircraft. Even low-mass explosive charges, especially when they are detonated in a confined space and at a short distance from exposed structure, can result in the weakening of that structure and the aircraft. This weakening, if intensified by aerodynamic forces, may lead to the complete destruction of the aircraft. Such charges are easy to conceal inside structural components—especially those that are important for maintaining aircraft control and structural integrity—making them a serious threat to air transport safety.

Despite the grave danger posed by explosives, the response of aircraft materials and structures to blast loading has not received appropriate attention within the research community. Aircraft fuselages are typically made of aluminum alloys, but previous research has focused on the effects of impulsive loading of flat or stiffened plates made of steel using differing geometries and boundary conditions [1–3]. In addition, in these studies, the air shock waves were generated in open space (free field explosions), and the intensity and type of load (uniform or localized) were varied by changing the mass of the explosive charge and its standoff distance. A comprehensive presentation of the work performed prior to 1989 and devoted to this topic is included in excellent review articles by Nurick et al. [4,5]. This review was updated in 2016 for work performed in subsequent years [6].

Jacob et al. [7] investigated the effect of varying the standoff distance of blast loads on the failure of mild steel plates. Damage to square, rectangular, and circular plates was found to be very similar when the plates were fixed along the perimeter and were subjected to uniformly distributed blast loading. Uniformly distributed loading was achieved by placing the blast source at a distance that exceeded the largest plate dimension. When the wave impulse had low magnitude, the plates underwent plastic deformation, with increasing permanent displacement of the central point of the plate as load intensity increased. A further increase in impulse loading resulted in the thinning of the plate at the boundary, followed by partial or complete peripheral tearing of the plate due to tension and shear at the supports. The fixed edges had a significant influence on the threshold impulse, resulting in circumferential tearing of the plate. Built-in and welded plates exhibited tears along the

* Corresponding author.
E-mail addresses: gaj@xtern-udvikling.dk (G.A. Jorgensen), wbinienda@uakron.edu (W.K. Binienda).

boundary at lower impulse values than clamped plates because, in the latter case, it was difficult to avoid in-plane movement of the plate, which delayed the tearing of the plates.

Geretto et al. [8] also performed experiments with test specimens constructed of mild steel. Three configurations, fully confined, vented, and unconfined, were subjected to blasts created by PE4 plastic explosive. For each of these configurations, three different mild steel thicknesses were tested, and a total of 94 experimental results were presented. For the fully confined configuration the charge mass was varied from 20 g to 70 g. Enough experiments were undertaken that test-to-test variation was characterized. Experimental deflections of less than one nominal plate thickness were considered within the experimental variation. For example, for a 3 mm thick target plate, a 3 mm variation was considered to be the test data scatter.

In internal blast loading, the structural walls are subjected to a transient component load and peak overpressure followed by a long quasi-static pressure. For a given internal geometry and given charge shape, orientation, and size, as well as the charge stand-off location, will affect both the loading, and as result, the structural response. Usually, close stand-off charge positions will lead to localization of loading and plastic deformation in the central region of a wall that is different from uniformly loaded permanent deformations. In these cases, instead of a single, symmetrical dome, deformed plates have a shape consisting of two domes: a global dome starting from the outer edge, and an inner dome with a larger curvature that is superimposed on the center of the larger global deformation. At higher impulses, thinning and cracking may first appear not on the plate periphery but in the central area of the plate, which leads to a hole being cut with a diameter close to that of the inner dome base (a condition known as "capping failure"). Further intensification of the loading causes the formation of cracks that propagate radially from the central cap, and the plate tears in a "petaling" mode. Remennikov et al. [9] studied the effects of such close-proximity blast loading on steel plates using both experiments and simplified modeling. Another simplified theoretical model, one that was limited to quasi-static pressure, was used to simulate a confined explosion, and once again the predictions were compared to test data; a good fit was achieved [10].

Successful modeling of explosive detonations has been performed using the Arbitrary Lagrangian–Eulerian (ALE) finite element technique for fluid–structure interaction [11,12]. In ALE, a charge detonation equation of state (EOS) commonly defines pressures in the Eulerian-represented fluid discretization, and the evolving pressure becomes a load on the Lagrangian-represented structure. Near-field explosion simulation results have been presented for trinitrotoluene (TNT) [13], and these results were compared with published test data [14]. The ALE method was also used to study the detonation of a spherical Composition C-4 charge in the air [15]. In this study, the wall-reflection effect was accurately reproduced.

Wang presented various techniques for ALE blast simulations that can be performed using the general-purpose finite element program LS-DYNA [16]. Mesh size and other parameters were assessed, and it was reported that overpressure was underpredicted by as much as 50%. In another study, it was shown that the accuracy of blast simulations can be improved if ALE is coupled with data from blast loading experiments [17]. Three methods in LS-DYNA are used to perform the blast analysis, and these techniques are compared in Rebelo and Cismaşiu [18]. The authors concluded that a Lagrangian approach using the empirical LOAD_BLAST_ENHANCED (LBE) feature was the most efficient method, but a higher maximum impulse was achieved using ALE coupled with the empirical blast load function.

Lomazzi et al. [19] compared efficiencies of three numerical methods: (i) coupled Eulerian-Lagrangian; (ii) uncoupled Eulerian-Lagrangian, and (iii) Analytical-Lagrangian. In the first two methods the blast wave properties are calculated numerically, and so require more computational effort than (iii), where the blast wave is treated analytically. Numerical method (ii) is less resource-demanding

than (i) due to the fact that it does not consider the influence of response of the structure. Purely analytical and empirical approaches were also presented, which are all more efficient than the numerical methods, and for some simple structures provide satisfactory accurate results.

Aluminum test plates were evaluated both experimentally and numerically by Langdon et al. [20]. The test configuration was a 1/6 scaled down model of a LD-3 aircraft luggage container. Although the LD-3 is constructed of Aluminum sheet riveted to a frame, the 1/6 mockup is mostly made of steel, except for an AA5754f22 Aluminum target plate. As some LD-3s are not fully confined, both vented and confined blasts were conducted. PE4 plastic explosive charge masses were varied from 10 g to 25 g. Unconfined experiments were also conducted; four with a 12 g charge mass, and a test-to-test variation of approximately 3 mm in the maximum permanent deflections was measured. Experimental data acquisition included Digital Image Correlation, and so deflection time histories were also recorded, and compared to LS-DYNA ALE simulations. The simulations were conducted using a 2 mm element size.

This article presents the results of an experimental and numerical investigation into the response of fully clamped, circular aluminum plates to confined air-blast loading. The confined test chamber was created by closing both ends of a thick-walled cylinder made of stainless steel with aluminum plates. The aluminum plates were subjected to impulsive loads generated by detonating cylindrical TNT charges with different masses from the same location in the chamber and also by detonating identical TNT charges at different positions in the chamber. In the first set of experiments, charges varying from 14 g to 50 g in mass were detonated from a central location. In the second set of experiments, all charges were 15 g in mass but were detonated at four different distances from the tested plate (40 mm, 50 mm, 70 mm, or 115 mm). The first objective of the experimental investigation was to find the parameters of TNT mass and standoff distance that would produce initial cracks in the tested plates but would not cause shattering or tearing at the boundary of the plates. The next objective was to measure the permanent deformation of the uncracked plates to aid in the development of an accurate LS-DYNA blast model. During some of the tests, pressure-time histories inside the chamber were also recorded.

In this investigation, the fluid air, the detonation, and the fluid–structure interaction in the experiments was simulated using ALE in LS-DYNA. The effects of finite element discretization, material properties, and loading definition on the numerical accuracy were assessed. The fluid (i.e., air) was represented in the Eulerian discretization, and the structure was modeled using Lagrangian finite elements. Established values from studies in the literature were the source of the EOS parameters used to define the explosive charge. This paper presents the validation that was performed for the comparisons of the permanent structural deformation and the onset of cracking that resulted when charge masses and charge positions were varied. The ability to predict the onset of cracking is particularly important in design to maintain structural integrity.

2. Experimental Setup

2.1. Test Chamber and Aluminum Plate Specimens

The test setup for the confined explosive loading of the aluminum plates is shown in Figure 1. The chamber was manufactured from a 250-mm-long tube of stainless steel with internal and external diameters of 255 mm and 327 mm, respectively. Aluminum plate test specimens with a thickness of 2 mm were placed on both ends of the tube and were clamped using a 30-mm-thick steel fastening ring that was fastened with a total of 24 high-strength bolts (8.8 class M10 bolts) tightened to a torque of 72 Nm. The clamping force produced an internal, small deformation towards the outer rim that provided additional locking force on the plate during its loading.

Fig. 1. Test setup for confined air-blast loading of aluminum plates: (a) Location of the chamber prior to testing; (b) End view of the assembly after mounting one end wall.

2.2. Explosive Charges

Cylindrical TNT charges were used to generate confined air blast loading on the tested plates. The TNT charges had a density of approximately 1.62 g/cm^3, and the charge masses were varied from 14 g to 50 g. The charges were generally 25 mm in diameter and had a central well that was 9 mm deep and 8 mm in diameter to allow the electric detonators to be inserted and positioned. (The two largest charges had a diameter of 30 mm.) The detonator consisted of an electric match embedded into 0.02 g of loose lead azide powder, under which 0.2 g of pressed lead azide was applied. The primary explosive was in contact with two layers of compressed pentaerythritol tetranitrate with a combined mass of 0.8 g. An approximate total mass of 1 g of TNT was estimated as the energetic equivalent of the explosive and firing composition of the detonator. The experiments clearly demonstrated that such detonators provide a sufficiently strong shock wave to ensure complete detonation of the TNT charges. The detonator and charge were enveloped in a thin layer of paper to impede charge fragments from impacting the test plates, as such impacts could initiate crack formation.

2.3. Instrumentation

Overpressure signals from a piezoelectric gauge (PCB Piezotronics, Model 113B22) located in the chamber wall were recorded with a digital storage scope. The measuring system was operated by its own internal trigger, which uses a pre-sampling technique.

Overpressure histories (Δp_{apr}) measured in the explosion chamber were approximated using Equation (1):

$$\Delta p_{apr} = a\left(1 - e^{-bt}\right) + ce^{-dt} \tag{1}$$

where a, b, c and d are constants, and where t denotes time. Equation (1) was used because it approximates well the results of the pressure measurement in the chamber. The overpressure–time relationships determined in this way can be regarded as the quasi-static pressure in the chamber. The overpressure at $t = 3$ msec was chosen for comparing the test loading intensity because it took 3 sec for the transient pressure to converge to oscillations about the quasi-static pressure (See Section 3.2).

The first part of Eq. (1) describes the pressure build-up due to the compression of the air filling the sensor socket (i.e., a 26.0-mm-long channel with a diameter of 9.0 mm) by shock waves generated by the detonation of the charge and reflected from the walls of the chamber. The second part of the equation (i.e., ce^{-dt}) in turn is responsible for the slow pressure drop in the chamber due to heat absorption by the metal walls of the chamber.

After integrating Equation (1), the following formula was obtained for the impulse $I(t)$ acting on the chamber walls:

$$I(t) = \int_0^t \Delta p_{apr}(t)dt = at + \frac{a}{b}e^{-bt} - \frac{c}{d}e^{-dt} - \frac{a}{b} + \frac{c}{b} \tag{2}$$

After determination of a, b, c and d from the approximation in Equation (1), the impulse (I_5) was calculated at 5 msec, which was the termination of the overpressure measurement. The impulse was calculated after the shock wave reached the sensor in the chamber wall by using Equation (2). The impulse values were also used as a measure of the loading intensity.

A Werth ScopeCheck 3D CNC multi-sensor coordinate measuring machine was used to determine the plate profiles after blast loading. The ScopeCheck 3D CNC machine has a measurement range of 400 mm in the X axis, 200 mm in the Y axis, and 200 mm in Z axis. The contour and profile in the area of greatest deformation was measured using a 50-mm-long Renishaw touch probe sensor. The probe measured the permanent deformation in increments of 0.01 mm.

2.4. Experimental Program

The experimental program included tests using 13 configurations. In the first set of experiments, TNT charges of 14 g, 15.5 g, 17.5 g, 20 g, 25 g, 30 g, 36 g, and 50 g in mass were located at a standoff distance of 115 mm from the test plate. The pressure sensor was placed at the end of a bore drilled into the cylindrical wall of the chamber at a position that was at the exact midpoint on the length of the steel pipe. The cylindrical wall thickness was 34.0 mm, and the sensor was screwed into the wall to a depth of 8.0 mm. Thus, the distance of the sensor's working surface from the inner wall of the chamber was 26.0 mm. The borehole had a diameter of 9.0 mm. A diagram showing the placement of the explosive charges, the detonator, and the pressure sensor inside the test chamber is presented in Figure 2.

A TNT charge of 14 g was used twice – in the first test, the charge was detonated in a chamber filled with air, while the second test was conducted in a nitrogen atmosphere (N_2) at an initial pressure of 0.1 MPa. In the second set of experiments, all charge masses were 15 g, and they were detonated at standoff distances of 115 mm, 70 mm, 50 mm, and 40 mm. For all tests, the explosive charges were positioned along the
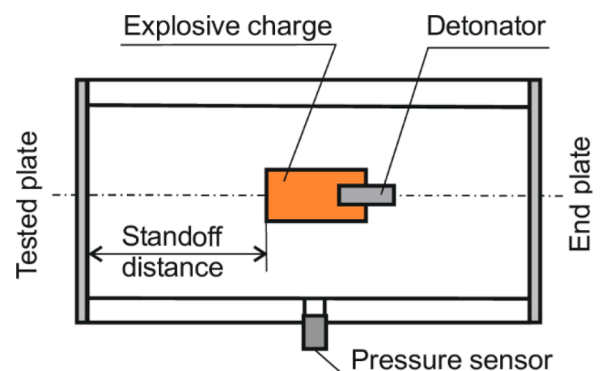

Fig. 2. Placement of the charge, detonator, and pressure sensor.

central axis of the chamber. Excluding the test denoted as #1/N$_2$, all the experiments were performed in air atmosphere at the initial ambient pressure. A summary of the test conditions is shown in Table 1.

Both the TNT mass and the estimated total explosive TNT equivalent mass (which includes both the TNT charge mass and the estimated detonator charge mass) are given in Table 1. The detonation was initiated from the side opposite to the measured test plate.

3. Analysis of Experimental Results

3.1. Response of Aluminum Plates to Confined Air-Blast Loading

The responses of the aluminum plates subjected to the confined air-blast loading from the TNT detonations were assessed by using the permanent plastic deformation values. Figure 3 shows the profiles of the non-cracked plates after centrally located explosive loading using charges ranging from 14 g to 30 g detonated at a standoff distance of 115 mm (Tests #1 through #6).

The maximum deflection due to the plastic deformation was found to occur at the midpoint of the plate and to increase linearly with the increase in TNT charge mass, as shown in Figure 3 (c). At charge masses lower than 20 g, the deformed plates have a single dome. For larger charges, inner domes atop the global domes are formed that have base radii equaling approximately 30 mm. In Tests #7 and #8 (36 g and 51 g of TNT, respectively), the plates were cracked along the area adjacent to the inner boundary of the support and had shattered into small pieces at the center.

The influence of standoff distance was determined in the second set of experiments (Tests #9 through #12) by keeping the charge mass at a constant 15 g of TNT. Photographs of the aluminum test plates from this set of experiments are shown in Figure 4 (a), and the permanently deformed profiles of the non-cracked plates (Tests #9 to #11) are shown in Figure 4 (b). From Fig. 4 (b), it can be noticed that the 15-g TNT charge mass generated a nonuniform permanent deformation when it was detonated closer than 70 mm to the exposed aluminum plate; in these tests, the deformation concentrated in the central area of the plate. Bringing the 15-g TNT charge another 20 mm closer to the plate (to a standoff distance of 50 mm) results in the appearance of an inner dome atop the main dome (Test #11 in Figure 4(b)). The impulse generated by the charge detonation at a 40-mm standoff distance (Test #12) was sufficient to tear the plate at the center with triangular sections or "petals" that folded away from the blast location, as shown in Figure 4 (a).

3.2. Blast Data Analysis

The pressure time histories, based on pressures measured in the test chamber following the detonations, allowed the characteristics of the blast waves to be determined. Figure 5(a) shows the experimental traces

and approximations generated by the centrally located TNT charges from Tests #1, #2, #3, #4, and #5. To show the influence of atmosphere (air or nitrogen at 0.1 MPa) on the pressure parameters in the chamber, in Figure 5(c), the measured overpressure and their approximations are also presented. The main oscillations in the records were caused by shock wave reverberations at the chamber walls, and their amplitudes decreased with time. Also visible are disturbances of smaller amplitude and higher frequency resulting from vibrations of the measuring system, reverberations of shock waves inside the sensor sockets, and turbulence of the gaseous medium.

The maximum permanent deflection, which occurs at the center point of the plate, is a linear function of the quasi-static pressure and the impulse (I_5), as shown in Figure 5(b) and 5(d), respectively. Neither the maximum overpressure nor the specific impulse calculated by integrating only the first peak of overpressure are correlated with the maximum permanent deflection. As can be observed in Figure 5(a) and 5(c), the forced excitation is approximately harmonic, and the period of the primary overpressure oscillation is approximately 0.25 msec. Therefore, the overpressure frequency can be estimated by:

$$\omega_f = \frac{2\pi}{\tau} \cong 25,000 \ \frac{rad}{sec} \tag{3}$$

where ω_f is the forcing frequency and τ is the period of the forced excitation. The first natural frequency of a circular plate can be calculated according to an equation in Leissa [21]:

$$10.2158 = \omega_n r^2 \sqrt{\frac{\rho}{D}}, \quad \text{where} \quad D = \frac{Eh^3}{12(1-\nu^3)} \tag{4}$$

where ω_n is the plate's first natural frequency, r is the plate radius, and h is the plate thickness; ρ is the density of the material, E is its elastic modulus, and ν is the Poisson's ratio. The plate diameter is 255 mm (thus, the radius is 127.5 mm), and the plate thickness is 2 mm. The elastic properties of aluminum are $= 2.6(10^{-9}) \frac{tonne}{mm^3}$, $E = 7.3(10^4) \frac{N}{mm^2}$, and $\nu = .33$. Consequently, an approximate first natural frequency can be calculated as follows:

$$D = 5.4614(10^4) \quad \text{and} \quad \omega_n = 2880 \frac{rad}{sec} \tag{5}$$

The ratio of the primary excitation frequency to the plate natural frequency is approximated as follows:

$$\frac{\omega_f}{\omega_n} \cong 8.7 \tag{6}$$

Therefore, the overpressure frequency is approximately nine times that of the primary natural frequency of the plate. With a forcing frequency almost nine times greater than the first natural frequency, a primary structural vibration mode does not have time to respond. The expected nondimensional amplification, with no damping, can be found using a simple equation from Thompson [22]:

Table 1
Description of Test Configurations used in the Experimental Program

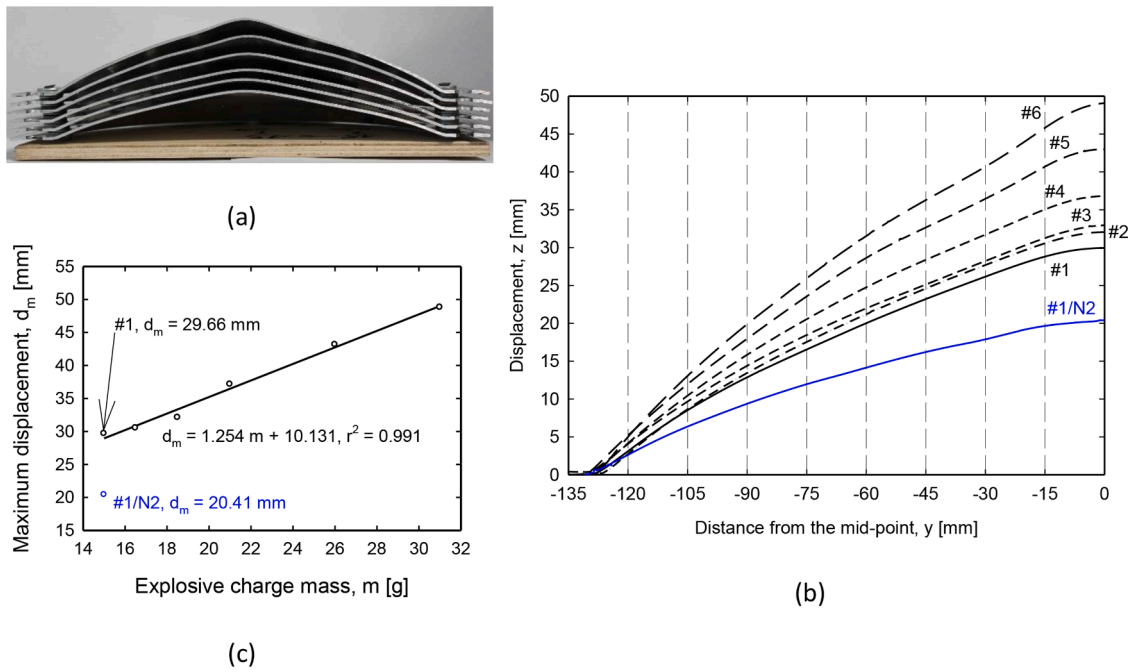| Test Number	TNT Mass, g	Estimated Total TNT Equivalent, g	Standoff Distance, mm	Pressure Measurement
#1	14.0	15.0	115	yes
#1/N$_2$	14.0	15.0	115	yes
#2	15.5	16.5	115	yes
#3	17.5	18.5	115	yes
#4	20.0	21.0	115	yes
#5	25.0	26.0	115	yes
#6	30.0	31.0	115	–
#7	36.0	37.0	115	–
#8	50.0	51.0	115	–
#9	15.0	16.0	115	yes
#10	15.0	16.0	70	–
#11	15.0	16.0	50	–
#12	15.0	16.0	40	–

Fig. 3. Non-cracked aluminum plates from the first set of experiments (Tests #1 to #6), with N_2 shown in blue: (a) photographs and (b) digitalized profiles of the plates; (c) plot showing the dependence of the maximal deflection on the explosive mass (approximation only for tests in air).
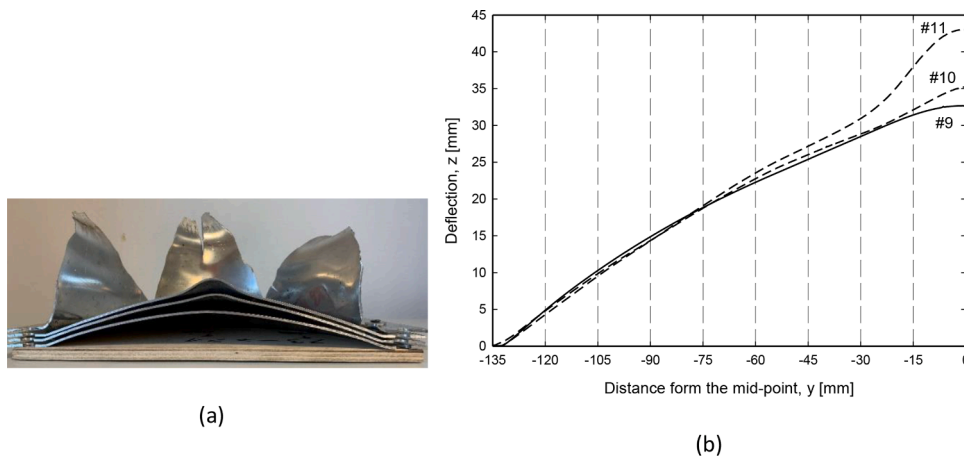

Fig. 4. Aluminum plates from the second set of experiments (Tests #9 to #11): (a) photographs and (b) digitalized profiles of the plates with a varying stand-off distance.

$$Amplification = \frac{1}{\sqrt{\left(1 - \left(\frac{\omega_f}{\omega_n}\right)^2\right)^2}} \cong .01 \qquad (7)$$

Only a small amplification of ~1% results from the primary quasi-harmonic excitation of the maximum overpressure, and so only a small portion of the plate's deflection results from high-frequency, quasi-harmonic excitation. Therefore, both the elastic and permanent deflection of the plate is primarily due to the quasi-static excitation. For this reason, the maximum permanent deflection of the plate is correlated with the quasi-static pressure, and the maximum overpressure does not correlate to the permanent deflection.

4. Simulation Input Parameters and Setup

4.1. The Material and Failure Model for Aluminum 2024-T3

Al 2024 is an aluminum alloy that is commonly used in the manufacture of aircraft fuselages. A highly reliable material and failure model is available for Al 2024-T351. However, Al 2024-T351 is not available at the desired thickness of 2 mm. Al 2024-T3 has the same chemical formulation as Al 2024-T351 and is produced using similar (but not identical) processing. The Al 2024-T3 processing differs to allow thinner plates to be produced, including plates at the desired thickness of 2 mm. Hence, the circular test plates used in these experiments were made of Al 2024-T3.

A material and failure model for Al 2024-T351 was developed as a part of the Federal Aviation Administration (FAA) Catastrophic Engine Failure Program [23]. This material and failure model is in the form of a MAT_224 input dataset for use in LS-DYNA [24]. The MAT_224 material
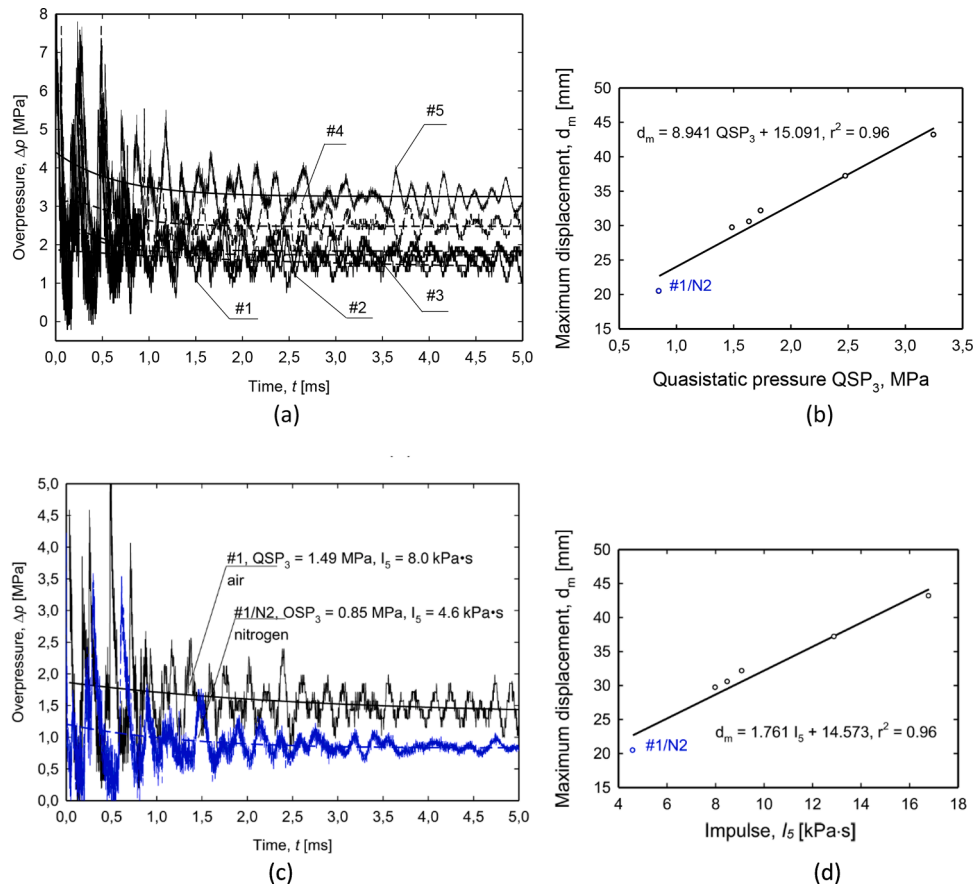
Fig. 5. Results for Tests #1, #1/N₂, #2, #3, #4, and #5: (a, c) Overpressure records and their approximations (with N₂ shown in blue). Dependence of the mid-point deflection on (b) quasi-static pressure and (d) total impulse.

model uses an approach that is similar to the Johnson–Cook material law, where the effects of strain rate and temperature are assumed to be multiplicative. The input parameter set for Al 2024-T351 has successfully been used multiple times in the simulation of complicated dynamic events involving penetration [23,25], and the material and failure model for this material was based upon and validated with data from an extensive experimental program [26–29]. The Al 2024-T351 material and failure law provides data from tests at temperatures ranging from 186 K to 933 K (the melting point of the material) and for strain rates between 10^{-4} 1/sec and 10^{7} 1/sec. It is noted that during the tests conducted in this study, no conditions occurred during the blast experiments that were outside the validated range of the material and failure model. Using a material model with proven reliability eliminates many of the uncertainties commonly encountered when interpreting the results of numerical simulations.

The Al 2024-T3 used in the manufacture of the test plates does not have identical material properties to the Al 2024-T351 used in the creation of the material model. The treatments to produce 2-mm-thick Al 2024-T3 plates and 12.70-mm-thick Al 2024-T351 plates are somewhat different and will result in different properties. In order to understand the differences between the Al 2024-T3 and the Al 2024-T351, quasi-static tensile testing was performed on samples of Al 2024-T3 [30]. Based on these test results, modifications were made to the Al 2024-T351 material and failure model in order to bring the model's input parameters close to the material properties of the AL 2024-T3 used in the blast tests. The mechanical property tests were simulated. Through iteration, it was found that by merely scaling the material model's input curve stress by a factor of 0.95, a close match to the stress–strain test data was created, an example of which is shown in Figure 6. The resulting model is shown in Figures 7(a) and 7(b) below.
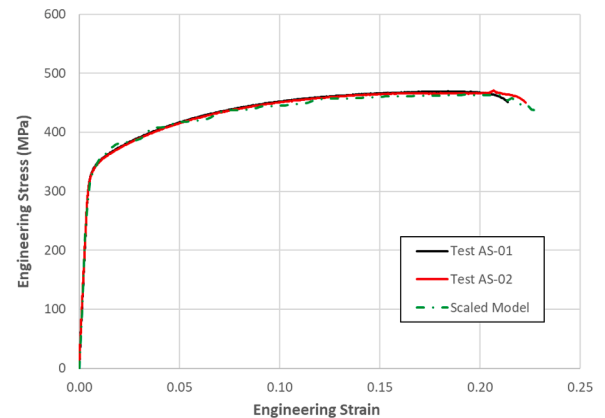
Fig. 6. Example Aluminum 2024-T3 scaled material model simulation results compared to test.
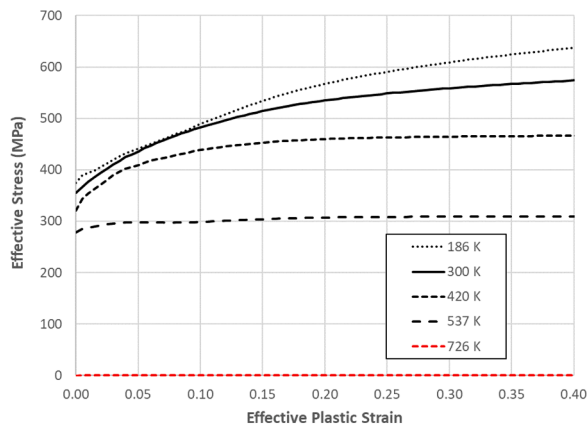
Strain hardening curves for strain rates between 0.0001 1/sec and 100000.0 1/sec are shown in Figure 7(a), and strain hardening curves for temperatures between 186 K and 933 K are shown in Figure 7(b).

As can be observed in Figure 7(a), Al 2024 displays little or no strain rate sensitivity at rates below 1000.0 1/sec. The vibrational response of the plates in the experiments is within the range of little or no strain rate sensitivity. Therefore, utilizing the Al 2024-T3 quasi-static tension data to modify the Al 2024-T351 strain hardening curves provides an appropriate model to evaluate permanent deformation in the blast tests.

Failure strains are dependent on temperature, strain rates, and the state of stress. In the Al 2024-T351 MAT_224 model, a stress-state
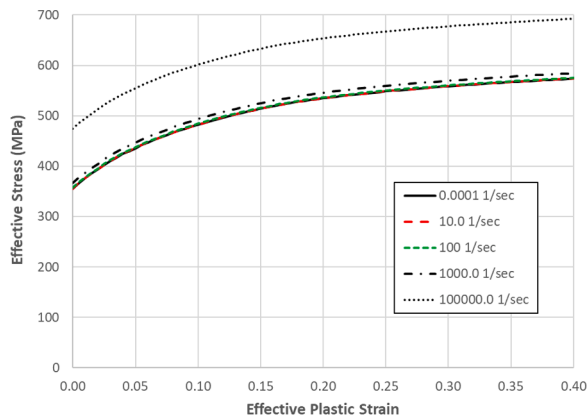
(a)

(b)

Fig. 7. Scaled Al 2024-T3 strain hardening curves for strain rates varying from 0.0001 1/sec to 100000.0 1/sec (a), and scaled Al 2024-T3 yield curves for temperatures of 186 K, 300 K, 420 K, 537 K, and 726 K. (The curves in Figure 7 (b) were obtained at quasi-static strain rates.)

dependent failure surface is used in conjunction with thermal and rate dependency. As a result, the stress–strain curves must be defined for the range of all possible failure strains, as the element erosion criteria is executed separately from the plasticity model. The Al 2024-T351 failure surface was scaled by a factor of 0.80 to match the Al 2024-T3 rupture in the uniaxial tensile tests. The identical material and failure properties were used for all simulations presented in this work. As will be shown later, the adjustments of the Al 2024-T351 based upon the Al 2024-T3 uniaxial tensile testing helped to provide an excellent match to the blast test data.

4.2. The Lagrangian and Eulerian Finite Element Meshes

The cylindrical structure of the assembled test specimen was represented by a quarter-symmetric model containing 63,677 shell elements. Shell elements were selected to provide consistency with the usual practice in the modeling of aircraft fuselage structures. A fully integrated shell element formulation was used in all the simulations. The model's Lagrangian finite element mesh is shown in Figure 8. The nominal element size was 2 mm × 2 mm. The steel cylinder and the bolted connections were represented using a rigid material model.

A Eulerian quarter-symmetric mesh consisting of 392,000 solid elements was used to represent the air, the explosive material, and the air blast as shown in Figure 9. The 1-point Arbitrary Lagrangian-Eulerian (ALE) multi-material solid element formulation was used. The nominal
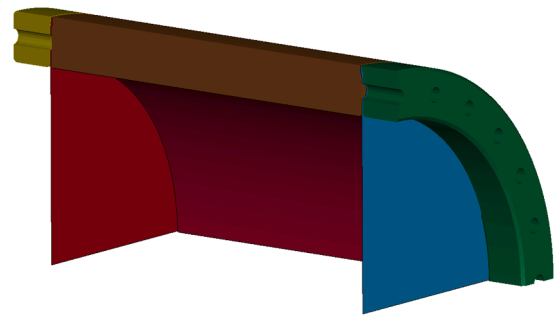

Fig. 8. Overview of the finite element mesh with the test plates and the frame parts.
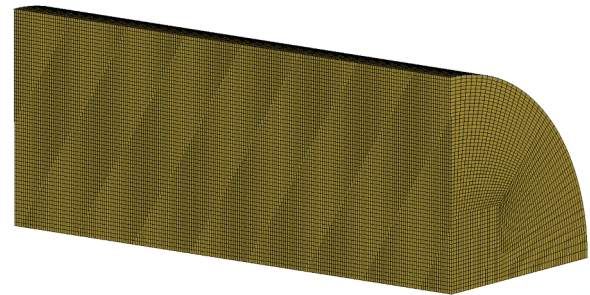

Fig. 9. Overview of the Eulerian mesh with 392,000 solid elements.

element size is 2.5 mm × 2.5 mm × 2.5 mm, which yields five elements that define the 12.5 mm charge radius. The mesh topology is of the "butterfly" type, which yields both an approximately consistent mesh size and an approximate match in mesh size between the Lagrangian and the Eulerian meshes. A consistent mesh size optimizes the fluid–structure interaction between the gases and the cylinder or test plates. ALE fluid–structure interaction was defined between the structure and the gases inside and outside of the cylinder. All ALE blast simulations were performed using the symmetric multi-processing (SMP) solver in LS-DYNA [31]. The SMP solver is preferred for blast simulations due to its consistency and reliability.

Arbitrary Lagrangian-Eulerian simulation results can depend strongly on the mesh size. The determination of an appropriate mesh size required a convergence study, which established the utilized nominal mesh size of 2.5 mm. Li et al. [32] also performed a convergence study, and determined convergence occurred at approximately 2 mm, although some of their modeled conditions were not identical to this study's. As mentioned earlier, the 2.5 mm mesh size results in 5 elements over the charge radius. Some best practice documents recommend using 10 elements over a charge radius. A simulation was conducted using a 1.25 mm nominal element size, which yielded ten elements defining the 12.5 mm charge radius. No significant difference in permanent displacements between the 2.5 mm and the 1.25 mm meshes resulted, and so there was little difference between using 5 elements or 10 elements over the charge radius. With the additional consideration that the smaller element mesh, and the necessary usage of the SMP solver, impractical simulation times resulted, a nominal mesh size of 2.5 mm was selected. Also note that the mesh size of the fluid/solid elements needs to be similar to the structure's shell element mesh size for the best functioning of the fluid–structure interaction (FSI) algorithm, and so the 2.5 mm nominal mesh size for the ALE elements is consistent with the 2 mm element mesh size of the Lagrangian elements.

Arbitrary Lagrangian-Eulerian simulation results can also depend strongly on the mesh orientation and fluid leakage. The mesh orientation for ALE simulation is typically a fully rectangular mesh; however, in this effort, a butterfly topology was adopted to facilitate the FSI with the

cylindrical structure. The FSI is based on a penalty function; here, a penalty pressure of 25 MPa for 1 mm of leakage was prescribed. Leakage is non-physical mass flow through the FSI and through the Lagrangian mesh, and it must be minimized in order for the ALE solution to be valid. The interaction between shell element meshed walls and the ALE solid elements representing the gas was created by using the *CONSTRAINED_LAGRANGE_IN_SOLID LS-DYNA, with the important parameters being shown in defined as shown in Table 2. The parameter options of the keyword that are not defined in Table 2 are where the defaults were selected, or where the parameter was not used.

The initial locations of the air and explosive materials within the Eulerian mesh can be defined using the LS-DYNA ALE capabilities. The *INITIAL_VOLUME_FRACTION_GEOMETRY keyword was used to define the size and location of the charge inside the ALE solid element mesh, as shown in Figure 10. Cylindrical charges with diameters of 25 mm (Tests #1 through #6) or 30 mm (Tests #7 and #8) were defined. The length of the cylindrical charge was determined from the diameter, mass, and density of TNT and from the volume of the detonator hole. In our simulations, only the TNT explosive mass was modeled, and the charge of the detonator was not explicitly included. The detonator hole, which had a diameter of 7.8 mm and a length of 9.3 mm, was modeled as a cylinder filled with air.

4.3. Charge and ALE Properties

The TNT was modeled using the *MAT_HIGH_EXPLOSIVE_BURN material model and the *EOS_JWL_AFTERBURN equation of state in LS-DYNA. The specific input parameters used in our model were adopted from those in a report by Dobratz and Crawford [33], which were originally derived from test data. The TNT material and equation of state properties are shown in Tables 3 and 4, respectively.

Several different advection methods are available in LS-DYNA ALE. Two of these methods—the van Leer method and the donor cell method—were utilized in this study. The van Leer method with Half-Index Shift is identified in LS-DYNA ALE as Advection Method 2, which is a second-order accurate algorithm and conserves internal energy. The donor cell method is a first-order accurate algorithm and is identified as Advection Method 3, where the Half-Index Shift has been modified to conserve total energy over each advection step.

In addition, both assumptions of afterburn and no afterburn were used in the simulations. Afterburn assumptions and calculations will be discussed in a later section. While simulations of blast loadings that involve charges on the order of 1 kg to 20 kg have been performed on a regular basis with LS-DYNA, very little simulation experience has been documented in studies that use charges as small as those considered in the experimental program (14 g to 50 g). As a result, it is important to determine the most appropriate advection algorithm and afterburn assumptions.
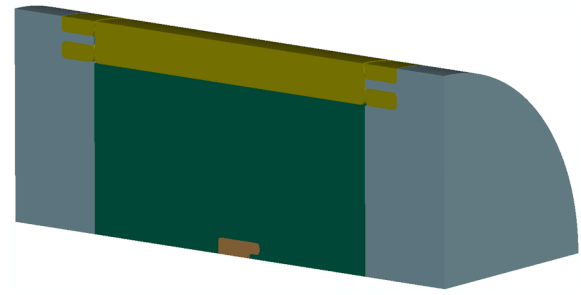

Fig. 10. Complete LS-DYNA model showing the ALE domain divided into TNT charge (*brown*), air inside the box (*green*), air outside the box (*blue*), and the wall of the steel cylinder (*yellow*), with the test plate to the right.

Table 3
Parameters for TNT for *MAT_HIGH_EXPLOSIVE_BURN

Mass Density (tonne/ mm³)	Detonation Velocity (mm/sec)	Chapman–Jouget Pressure (MPa)	Beta Burn-Flag
1.63 E-9	6.93 E+6	2.1 E+4	Programmed Burn Only

Table 4
Parameters for TNT using *EOS_JWL_AFTERBURN

A (MPa)	B (MPa)	R₁	R₂	Omega	Detonation Energy per Unit Volume (MPa)	Initial Relative Volume
3.712 E+5	3231.0	4.15	0.95	0.30	7000.0	1.0

5. Simulation Results

5.1. Centered Charge Initial Simulation Results

Simulations of the tests with the centered charges were performed using the inputs discussed in the previous section. The first set of numerical simulations assumed that no afterburn occurred. The subset of tests which were simulated in this initial set, along with the charge dimensions, are shown in Table 5. Only the TNT charge mass was included in the simulation, and the estimated detonator mass of 1 g used in the experimental program was not modeled.

As Test #6 (with a charge mass of 30 g) had the highest charge mass that produced no cracks in the test plates, the results of this test simulation will be discussed in greater detail. Figure 11 shows the evolution of the simulated blast pressure within the cylindrical test specimen in Test #6. For the initial centered-charge simulations, the donor cell method (total energy conserving, Advection Method 3 in LS-DYNA) was used.

The resulting permanent deformation of the test plate from Test #6 are compared to the numerical predictions in Figure 12. The numerical predictions produced no cracks in the plate, which is consistent with the test results. A 3% overprediction of the plastic deformation at the center of the plate was observed as well as small underpredictions of the deformations towards the edges. The plastic strain was no longer increasing after approximately 0.0004 sec, although vibratory response was continuing. The deformed shape of the simulated aluminum test plate at *t* = 0.0006 sec is shown in Figure 13.

For all explicit analyses, the energy balances must be checked to determine if energy is being non-physically created or lost during the simulation [34]. In addition, the leakage occurring during an ALE simulation should also be checked to ensure that the fluid mass loss is minimal. Figure 14(a) shows the energy balance and Figure 14(b) shows

Table 2
ALE Parameters for used for Fluid–Structure Interaction.

LS-DYNA Label	LS-DYNA Value	Fluid-Structure Interaction Option
NQUAD	4	4 × 4 coupling points distributed over each Lagrangian surface segment
CTYPE	4	Penalty coupling for shell and solid elements
DIREC	2	Normal direction coupling in compression only
PFAC	Curve	The coupling pressure is a function of the penetration Penetration = 0 mm, Pressure = 0 MPa Penetration = 5 mm, Pressure = 125 MPa
NORMTYP	1	Penalty coupling force direction normal vectors are interpolated from the segment normal vectors
DAMP	0.2	Damping factor of .2 for penalty coupling
ILEAK	2	Strong coupling leakage control

Table 5
Centered Charge Simulation Summary.

Test Number	Simulation Charge Mass (g)	Charge Height (mm)	Charge Diameter (mm)	Standoff Distance (mm)	Failure Result
#1	14.0	18.40	25.0	115.0	Intact
#2	15.5	20.28	25.0	115.0	Intact
#3	17.5	22.78	25.0	115.0	Intact
#4	20.0	25.90	25.0	115.0	Intact
#5	25.0	32.15	25.0	115.0	Intact
#6	30.0	38.39	25.0	115.0	Intact
#7	36.0	31.87	30.0	115.0	Fractured
#8	50.0	44.02	30.0	115.0	Fractured

$t = 0.0$ sec

$t = 0.0002$ sec

$t = 0.0003$ sec

$t = 0.0004$ sec

$t = 0.0005$ sec

$t = 0.0006$ sec
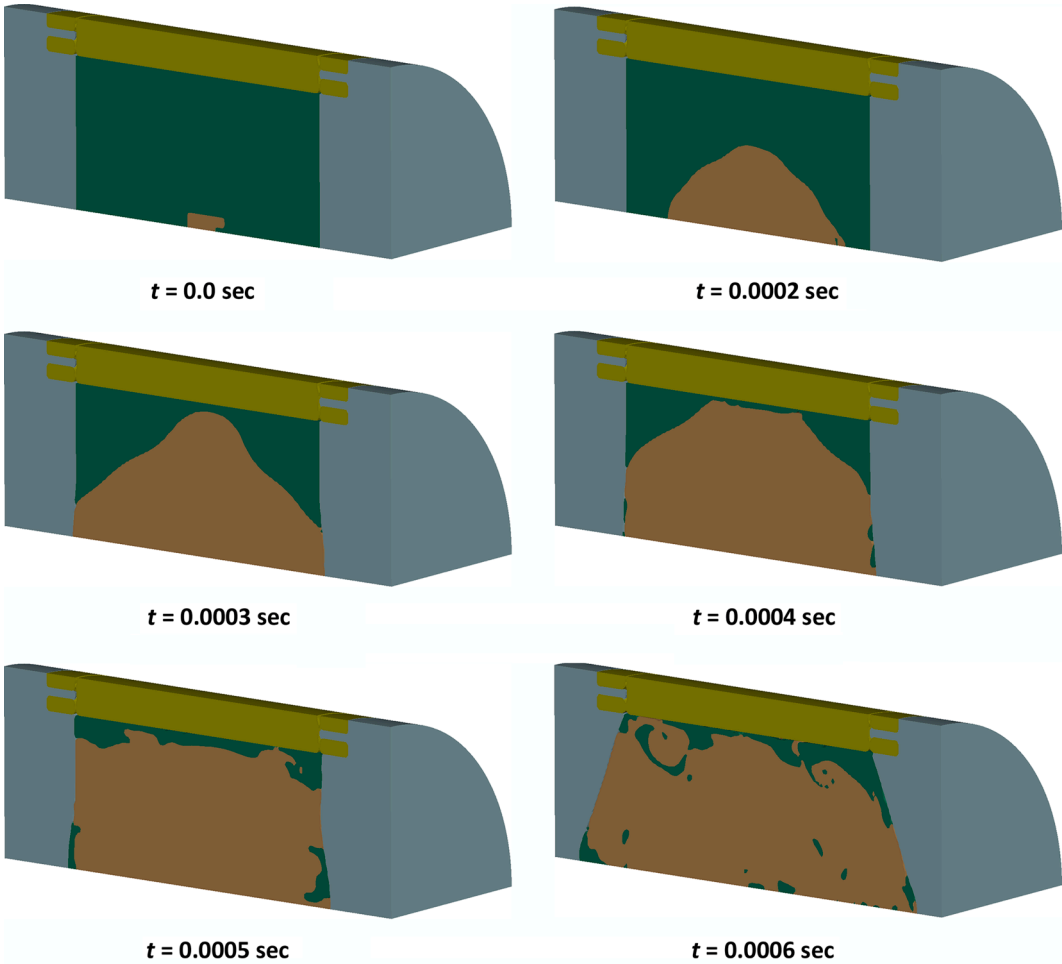
Fig. 11. Constituent distribution and specimen deformation in the simulation of Test #6, in which a charge mass of 30 g was used.
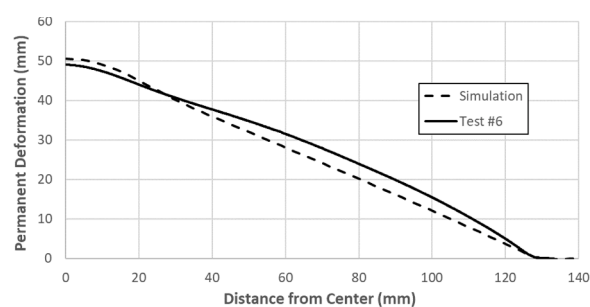
Fig. 12. The permanent deformation of the test plate, compared to the numerical predictions for the simulation Test #6 (with a 30-g charge).
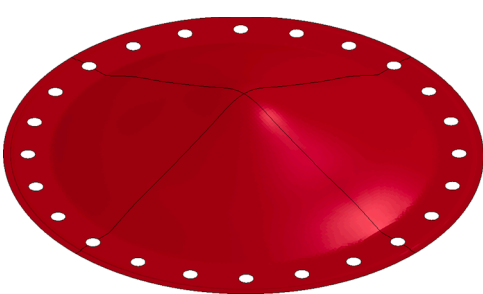
Fig. 13. The deformed shape of the test plate at $t = 0.0006$ sec in the simulation of Test #6, in which a 30-g charge mass was used.
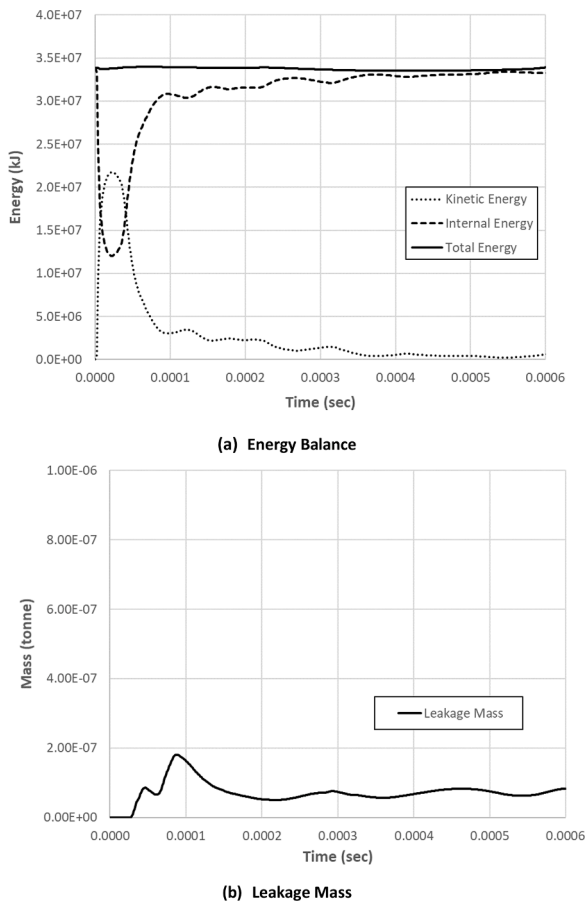
(a) Energy Balance

(b) Leakage Mass

Fig. 14. Numerical checks of the Test #6 simulation, in which a charge mass of 30 g was used.

the leakage of the Test #6 simulation. Note that no significant energy is being created or lost, and the fluid mass loss is on the order of 10^{-7} tonne (0.1 g), which is also acceptable.

In Figure 15, the permanent deformations from the centered charge test simulations are compared with the experimental results. Simulations for tests using 14 g to 30 g of TNT (Tests #1 through #6), are shown. As previously stated, the donor cell method (Advection Method 3, first order accurate, total energy conserving) was used in all of these simulations, with no afterburn. The same numerical checks shown for the Test #6 simulation (Figure 14) were also performed for the other test
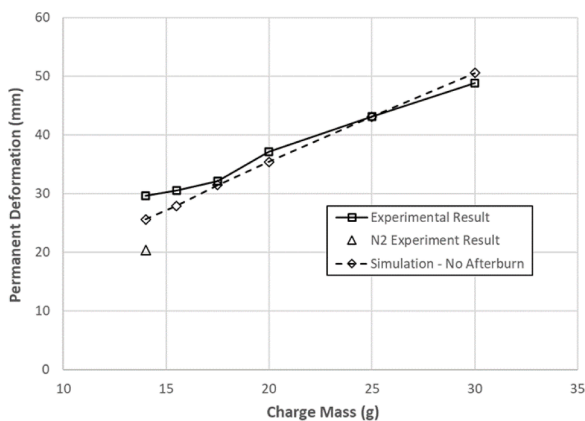

Fig. 15. The maximum displacements in the aluminum plates for Tests #1 through #6, in which the charges were centered and the charge masses were varied.

simulations. Again, all simulations were shown to be numerically reliable. The permanent deformations in the simulated detonations for charges of 17.5 g and greater are within 5% of the test deformations. The permanent deformations in the simulated detonations are underestimated for charges smaller than 17.5 g when compared to the blast experiments in air. The slope of the deformation versus charge line increases at 17.5 g of TNT in the air experiments, but the slope of the same line of the simulations does not change. The permanent deflection of the 14-g test (Test #1) is overestimated when compared to the approximate permanent deformation measurement of the test using the same charge mass conducted in N_2 atmosphere.

Figure 3(c) previously demonstrated a linear trend in the permanent deflections, with each test deviating from that linear trend to varying degrees. These differences demonstrate a degree of randomness in the permanent deformations of the test plates. Performing test repeats to establish significant statistical distributions was beyond the scope of this project. Stochastic variation in these permanent deformations is due to some combination of variations in the Al 2024-T3 plate material properties, plate boundary conditions (including bolt tension and friction), explosive charge density and mass, ambient air pressure and temperature, and detonation physics. Despite this degree of randomness, there is a clear difference between the results in the test where oxygen was available for afterburn and those for the N_2 atmosphere test where no afterburn was possible. This demonstrates that afterburn occurred in the primary series of experiments, despite the small charge masses. Note that the detonation physics could also have been affected by the oxygen-free environment in the N_2 test.

In both the tests and the simulations, no fracture occurred with a charge mass of 30 g of TNT (Test #6), but fracture did occur with a charge mass of 36 g (Test #7). Permanent deformation values for the 36-g charge (Test #7) and the 50-g charge (Test #8) are not shown in Figure 15, as cracks and substantial failure occurred in these experiments. An image of Test #7, which used a charge mass of 36 g, is shown in Figure 16. The same numerical checks shown in Figure 14 for the Test #6 simulation were performed (not shown), and again this simulation was demonstrated to be numerically reliable. In the simulation, fracture occurred in the center and at the edge of the plate at 0.00039 msec. In the test, there was no fracture initiated at the exact center, and the fracture along the edge was complete.

Figure 17 presents the plate in the simulation of the 50-g charge in Test #8 (at 0.0006 sec) and a photograph of the deformed plate for Test #8 (post-test). The shape of the plate from the simulation is similar to what was observed in the experiment, with substantial failure. In both cases, the plate fractures completely at its base and develops cracks from the center.

The set of simulations using no afterburn matched the results of tests for charge masses of 17.5 g and greater with reasonable agreement. The differences in the permanent deformations between the simulations and tests with charge levels between 17.5 g and the crack onset are less than 5%. More importantly, the charge that caused the onset of fracture was predicted accurately. The numerical checks indicated valid solutions in all simulations. Part of the difference between the simulation permanent

Fig. 16. The simulation at 0.0006 sec for Test #7 using a charge of 36 g (*left*) and the post-test deformation of the plate from Test #7 (*right*) both resulted in fracture.
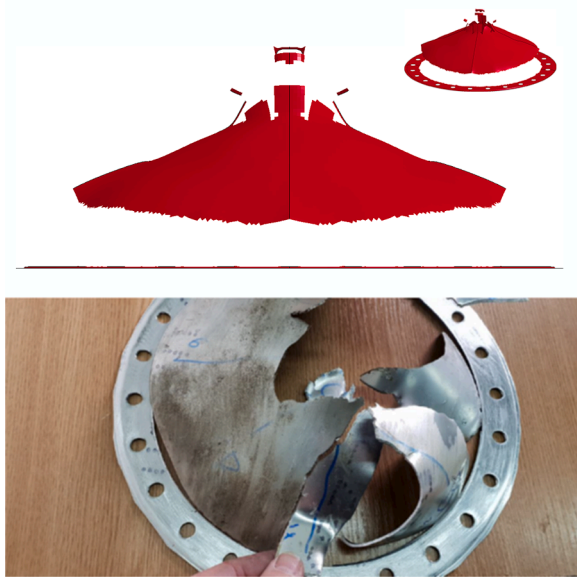
Fig. 17. The simulation of the plate in Test #8 at 0.0006 sec (*top*) and the post-test plate for Test #8 using a charge mass of 50 g (*bottom*) both resulted in substantial failure. Note that in both cases, the plate has fractured along the entire perimeter.

deformations and those of the primary test series charge masses of 14 g and 15.5 g are due to non-modeling of the afterburn.

5.2. Afterburn Correlation and Simulation Results

As demonstrated by the test performed in the N_2 atmosphere (#1/ N_2), and discussed in the previous section, afterburn clearly occurred in tests performed in an air atmosphere. An investigation was conducted to determine if including a realistic amount of additional energy in the numerical simulations, produced by afterburn, would improve the correlation of the 14 g and 15.5 g charge mass simulation results to the experiments. The amount of afterburn required to improve the correlation to these two tests was calculated, and how this additional energy would affect the predicted permanent displacements of the other tests was also assessed.

First, the maximum amount of afterburn energy which could be produced by the air and oxygen in the test cylinder was calculated. Each cylindrical test specimen contained approximately 16 g of air. Since air is 23.7% oxygen by mass, approximately 3.8 g of oxygen was contained in the test specimen, which is approximately 0.12 mole of oxygen. The combustion equation for TNT is as follows:

$$4\ C_7H_5N_3O_6 + 21\ O_2 \rightarrow 28\ CO_2 + 6\ N_2 + 10\ H_2O \tag{8}$$
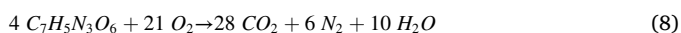
Thus, 21 moles of oxygen are required to burn 4 moles of TNT. With 0.12 mole of oxygen, a total of 0.023 mole (5.22 g) of TNT could be potentially be burnt. How much TNT is actually burnt will depend upon the amount of locally available oxygen—which, in turn, depends on the turbulent mixing of the gases, the temperature, and other variables.

The heat of combustion for TNT is 14.5 kJ/g and the heat of detonation is 4.184 kJ/g, resulting in a difference of 10.316 kJ/g. The maximum additional energy that could be produced by afterburn can thus be calculated by multiplying the theoretical maximum TNT afterburn mass (5.22 g) by the difference in heat:

$$\left(10.316\ \frac{kJ}{g}\right)(5.22\ grams) = 53.85\ kJ. \tag{9}$$

Second, simulations of Test #1 were repeated with varying percentages of afterburn until an approximate match to the permanent displacements was obtained. In these simulations, the advection method

was changed to the van Leer method with Half-Index Shift (Advection Method 2 in LS-DYNA), which is second-order accurate and internal energy conserving. The resulting afterburn percentage of 26% corresponds to an afterburn mass of 3.16 g and an afterburn energy of 32.64 kJ, which is well below the theoretical maximum. So, this amount of afterburn energy is physically feasible.

If an afterburn of 3.16 g of TNT was approximately consistent for each charge size (assuming primary afterburn dependence is on the amount of oxygen in the cylinder specimen), this afterburn mass would increase the energy ~56% for the 14-g charge mass (Test #1). As a comparison, the afterburn parameters for the test simulations using a 14-g charge mass (Test #1) and a 30-g charge mass (Test #6) are shown in Table 6.

Third, all of the centered charge simulations were repeated using the same assumed afterburn mass and the Half-Index Shift advection method. Figure 18 summarizes the results obtained when using afterburn and Advection Method 2.

As can be seen in Figure 18, including a small amount of afterburn greatly improves the match of the simulations to the tests using small charge masses. The addition of afterburn does not greatly influence the simulations of the tests that use larger charges; it slightly improves the already good match. In addition, the amount of TNT needed to produce fracture in the simulations is not affected by the addition of afterburn.

We cannot state for certain the exact amount of afterburn that was present in the experiments. The very close match of the afterburn simulations to the primary test series was partially a result of correlation. Given the previously discussed stochastic component of the permanent deformations, the match should not be construed to prove that a specific afterburn mass occurred. That said, the assumed amount of afterburn is plausible with respect to the amount of oxygen available in the cylindrical test specimen.

5.3. Simulation Results for Tests where the Standoff Distance was Varied

In this investigation, a second series of tests was conducted in which different standoff distances were used and a small charge mass of 15 g was adopted. The calculated afterburn mass of 3.16 g was adopted for the varying standoff distance set of simulations. The tests were simulated using the van Leer method with Half-Index Shift (Advection Method 2). Higher penalty stiffnesses for the fluid–structure interaction algorithm were used to minimize leakage resulting from the closeness of the charges to the plate. For penetrations of 5 mm, Test #10 the penalty pressure was increased to 250 MPa, and for Test #11 the penalty pressure was increased to 500 MPa. The second series of tests and the failure results are summarized in Table 7. Test #9, which used a standoff distance of 115 mm, was not simulated.

It can be seen from Table 6 that the critical distance between the charge and the plate that results in fracture from the detonation of a 15-g charge was well captured by the numerical simulations. The permanent displacements from Test #10 (with a standoff distance of 70 mm) are shown in Figure 19. It can be seen in this figure that the permanent deformation from the simulations somewhat underpredict the corresponding experimental displacements.

Figure 20 shows a comparison of the profiles of the test plate and the simulation of Test #11, which had a standoff distance of 50 mm. The double dome shape from the close proximately charge, which was anticipated from results reported in published literature, is clearly visible.

As can be seen in Figure 21, the match of the displacement profiles for Test #11 is shown. In the region of the second, smaller central dome, the experimental permanent deflection is greater. For the small secondary dome, the utilized mesh size of 2 mm was likely too coarse to obtain an accurate prediction. The previously discussed mesh convergence study was not performed by simulating this particular test. While a smaller mesh size would improve the numerical predictions of the maximum permanent deflection of the secondary dome, it would result

Table 6

Afterburn Parameter Summary

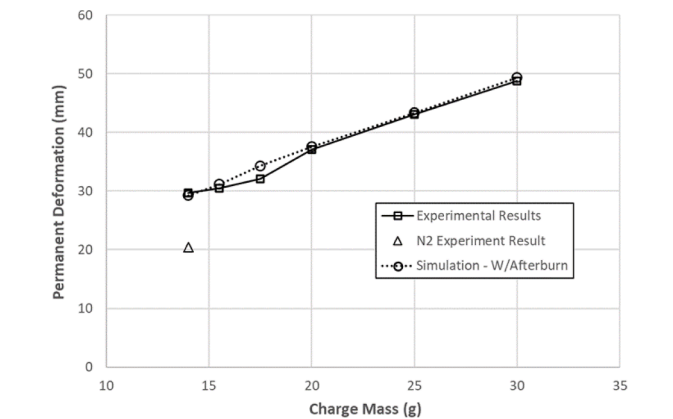| Test Number	Charge Mass (g)	Detonation Heat (kJ)	Calculated Afterburn Mass (g)	Calculated Afterburn Heat (kJ)	Calculated Afterburn Used	Theoretical Maximum Afterburn
#1	14	58.58	3.16	32.63	55.7%	91.9%
#6	30	125.52	3.16	32.63	26.0%	42.9%

Fig. 18. Maximum permanent displacements for Tests #1 through #6 using Advection Method 3 with no afterburn (*indicated as diamonds*) and using Advection Method 2 with afterburn (*indicated as circles*).

Table 7

Summary of Tests and Simulations where Standoff Distance was Varied

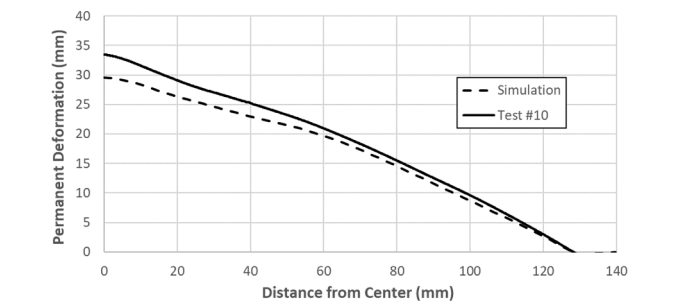| Test Number	Charge (g)	Standoff Distance (mm)	Test Failure Result	Simulation Failure Result
#10	15	70	Intact	Intact
#11	15	50	Intact	Intact
#12	15	40	Fractured	Fractured

Fig. 19. Permanent displacements resulting from a standoff distance of 70 mm and a 15-g charge (Test #10), with the experimental results compared to the numerical predictions.
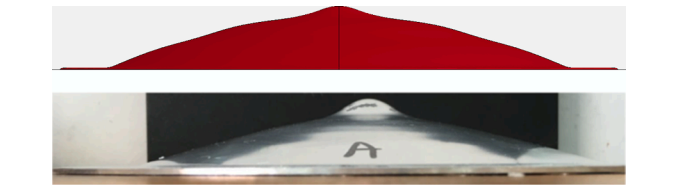

Fig. 20. The numerical displacement profile for Test #11, which used a standoff distance of 50 mm and a 15-g charge (*top*). Final displacement of the plate in Test #11 (*bottom*).
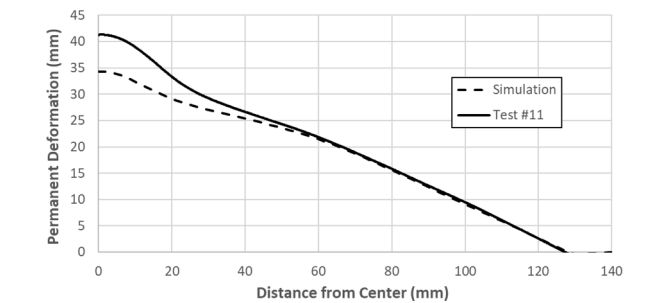

Fig. 21. The permanent displacements resulting from a standoff distance of 50 mm and a 15-g charge (Test #11), with experimental results compared to the numerical predictions.

in much longer simulation run times and, thus, would be impractical for a full-scale airframe simulation.

For a standoff distance of 40 mm, the simulation correctly predicted the cracks and massive fracture observed in the plate for Test #12. Figure 22 shows the simulation profile at a point early in the simulation (at 0.0002 sec) that was prior to the propagation of the initial crack. Beyond this time, the crack propagation was no longer symmetric, and it could not be analyzed with the quarter-symmetric model. The post-test experimental result for these blast conditions is also shown in Figure 22. Overall, the match between the simulations and the experimental results of the varying standoff distance tests using a 15-g charge, in particular the onset of failure, is acceptable.

6. Summary and Conclusions

An experimental and numerical investigation was conducted to examine the response of 2-mm-thick, 255-mm-dimeter Al 2024-T3 plates that were subjected to air blast loading. The test specimen was a 250-mm-long, thick-walled stainless-steel cylinder with Al 2024-T3 plates at the two ends. Detonation of TNT charges with varying masses at several axial positions in the chamber created the blast overpressure loading. In the first set of experiments, charges ranging from 14 g to 50 g in mass were detonated at a central location in the
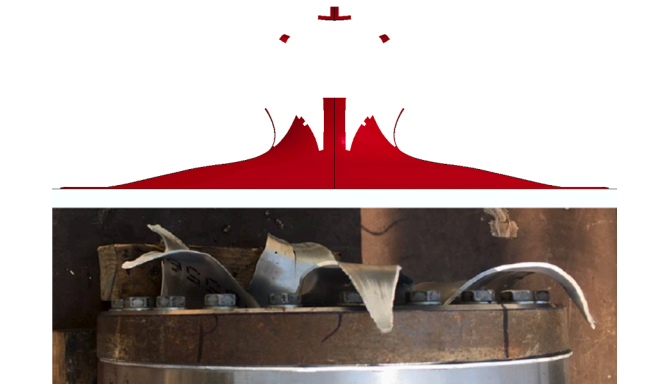

Fig. 22. Numerical simulation displacement results at 0.0002 sec (which was early in the simulation response) for the simulation of Test #12 using a standoff distance of 40 mm and a 15-g charge (*top*). Post-test image of the plate in Test #12 (*bottom*).

chamber. In the second set of experiments, all charges were 15 g in mass, and they were detonated at different standoff distances. A separate test with a sealed test chamber and a N_2 (no oxygen) atmosphere confirmed the presence of afterburn in the other tests.

The set of simulations that did not include the effects of afterburn were compared to the experimental results, with generally good agreement. However, for charge masses of less than 17.5 g, the permanent deflections were somewhat underpredicted with no afterburn. The simulations using a different advection method and with the addition of afterburn matched well with all of the permanent deformations in the set of experiments with varying charge mass. The simulations of the varying standoff distances somewhat underpredicted the permanent displacements. The onset of rupture was predicted correctly for both sets of experiments and numerical parameters. Considering that few previous blast simulation efforts on aluminum have been published, using charge masses as small as those considered in this project, this result was encouraging.

A primary goal of this investigation was to determine the explosive mass and standoff distance needed to produce initial cracks in the tested aluminum plates. In all simulations, the results of the numerical simulations matched the experiments well. This general agreement demonstrates the ability of carefully performed numerical simulations to accurately predict the onset of fracture without iterations. However, this success in obtaining realistic results was possible due to the availability of a reliable material and failure model for the structural material that was exposed to the blast. Developing such a material and failure model can represent a major effort—both in terms of conducting the experiments to obtain a sufficient amount of data and the effort required for numerical calibration and validation. A second condition for obtaining realistic results is that the mesh must be convergent. Finally, as this type of numerical simulation is CPU-intensive, a hardware environment with a sufficiently large number of cores will generally be required.

The capability to predict the effects of low-mass explosive charges on full-scale airframe structures is an important tool in both evaluating incidents and in design to maintain control and structural integrity. The presented numerical approach, including the finite element discretization, material model and blast modeling methodology, is a template for analyzing potential blast events in full-scale aircraft. Full-scale aircraft blast simulations can contribute both to incident evaluation and maintaining air transport safety.

CRediT author statement

Kelly S. Carney: Conceptualization, Software, Writing - Original Draft, Writing - Review & Editing. **Paul DuBois:** Conceptualization, Software, Writing - Original Draft. **Stanisław Cudziło:** Conceptualization, Funding acquisition, Investigation, Writing - Review & Editing. **Glenn A. Jorgensen:** Conceptualization, Funding acquisition, Investigation. **Wieslaw K. Binienda:** Conceptualization, Funding acquisition, Supervision, Writing - Original Draft, Writing - Review & Editing.

Declaration of Competing Interest

The authors declare that they have no known competing financial interests or personal relationships that could have appeared to influence the work reported in this paper.

Data Availability

Data will be made available on request.

Acknowledgements

References

[1] Langdon GS, Chung Kim Yuen S, Nurick GN. Experimental and numerical studies on the response of quadrangular stiffened plates. Part II: Localised blast loading. International Journal of Impact Engineering 2005;31:85–111. https://doi.org/10.1016/j.ijimpeng.2003.09.050.

[2] Ostadhossein H, Lotfi S. Performance of infill stiffened steel panel against blast loading. Latin American Journal of Solids and Structures 2018;15(2):e16. https://doi.org/10.1590/1679-78254429.

[3] Zahrai SM, Lotfi S. Study on transferred impulse and response of steel plate walls under various impulsive loading considering mesh size effects. Theoretical and Applied Vibration and Acoustics 2018;4(1):65–80. https://doi.org/10.22064/tava.2018.79933.1094.

[4] Nurick GN, Martin JB. Deformation of thin plates subjected to impulsive loading – A review; Part I: Theoretical considerations. International Journal of Impact Engineering 1989;8:159–69. https://doi.org/10.1016/0734-743X(89)90014-6.

[5] Nurick GN, Martin JB. Deformation of thin plates subjected to impulsive loading – A review; Part II: Experimental studies. International Journal of Impact Engineering 1989;8:171–86. https://doi.org/10.1016/0734-743X(89)90015-8.

[6] Chung Kim Yuen S, Nurick GN, Langdon GS, Iyer Y. Deformation of thin plates subjected to impulsive load: Part III – An update 25 years on. International Journal of Impact Engineering 2016;107:108–17. https://doi.org/10.1016/j.ijimpeng.2016.06.010.

[7] Jacob N, Nurick GN, Langdon GS. The effect of standoff distance on the failure of fully clamped circular mild steel plates subjected to blast loads. Engineering Structures 2007;29:2723–36. https://doi.org/10.1179/1743280413Y.0000000028.

[8] Geretto C, Chung Kim Yuen S, Nurick GN. An experimental study of the effects of degrees of confinement on the response of square mild steel plates subjected to blast loading. International Journal of Impact Engineering 2015;79:32–44. https://doi.org/10.1016/j.ijimpeng.2014.08.002.

[9] Remennikov A, Ngo T, Mohotti D, Uy B, Netherton M. Experimental investigation and simplified modeling of response of steel plates subjected to close-in loading from spherical liquid explosive charges. International Journal of Impact Engineering 2016;101:78–89. https://doi.org/10.1016/j.ijimpeng.2016.11.013.

[10] Feldgun VR, Karinski YS, Edri I, Yankelevsky DZ. Prediction of the quasi-static pressure in confined and partially confined explosions and its application to blast response simulation of flexible structure. International Journal of Impact Engineering 2016;90:46–60. https://doi.org/10.1016/j.ijimpeng.2015.12.001.

[11] U.S. Department of the Army. Fundamentals of Protective Design for Conventional Weapons. Washington, D.C., U.S.A.: Technical Manual; 1998. p. 5.1–3. TM5-855-1.

[12] Hirt CW, Amsden AA, Cook J. An Arbitrary Lagrangian–Eulerian Computing Method for all flow speeds. Journal of Computational Physics 1974;14(3):227–53. https://doi.org/10.1016/0021-9991(74)90051-5.

[13] Cheng D-S, Hung C-W, Pi JW. Numerical Simulation of Near-Field Explosion. Journal of Applied Science and Engineering 2013;16(1):61–7. https://doi.org/10.6180/jase.2013.16.1.09.

[14] U.S. Department of the Army. Structures to Resist the Effects of Accidental Explosions. Washington, D.C., USA: U.S. Department of the Army; 1990. p. 1–1867. Technical Manual, TM5-1300.

[15] Alia A, Souli M. High explosive simulation using multi-material formulations. Applied Thermal Engineering 2006;26(10):1032–42. https://doi.org/10.1016/j.applthermaleng.2005.10.018.

[16] Wang J. Simulation of landmine explosion using LS-Dyna3D Software: Benchmark work of simulation of explosion in soil and air. Fishermans Bend, Australia: Department of Defense, DTSO Aeronautical and Maritime Research Laboratory; 2001. Technical Report DSTO-TR-1168.

[17] Slavik TP. A Coupling of Empirical Explosive Blast Loads to ALE Air Domains in LS-DYNA. IOP Conference Series: Materials Science and Engineering 2010;10:012146. https://doi.org/10.1088/1757-899X/10/1/012146.

[18] Rebelo HB, Cismaşiu C. A Comparison between Three Air Blast Simulation Techniques in LS-DYNA. In: Proceedings of 11th European LS-DYNA Conference 2017; 2017. Salzburg, Austria.

[19] Lomazzi L, Giglio M, Manes A. Analytical and empirical methods for the characterization of the permanent transverse displacement of quadrangular metal plates subjected to blast load: Comparison of existing methods and development of a novel methodological approach. International Journal of Impact Engineering 2021;154:103890. https://doi.org/10.1016/j.ijimpeng.2021.103890.

[20] Langdon GS, Kriek S, Nurick GN. Influence of venting on the response of scaled aircraft luggage containers subjected to internal blast loading. International Journal of Impact Engineering 2020;141:103567. https://doi.org/10.1016/j.ijimpeng.2020.103567.

[21] Leissa AW. Vibration of Plates. Washington, DC, USA: National Aeronautics and Space Administration; 1969. NASA SP-160.

[22] Thompson W. Theory of Vibration with Applications. Englewood Cliffs, USA: Prentice-Hall; 1972.

[23] Emmerling W, Altobelli D, Carney K, Pereira M. Development of a New Metal Material Model in LS-DYNA® Part 1: FAA, NASA, and Industry Collaboration Background. DOT/FAA/TC-13/25, P1. Washington, DC, USA: U.S. Dept. of Transportation, Federal Aviation Administration; 2015.

[24] Park C-K, Carney K, Du Bois P, Cordasco D, Kan C-D. *Aluminum 2024-T351 Input Parameters for *MAT_224 in LS-DYNA*, DOT/FAA/TC-19/41, P1. Washington, DC, USA: U.S. Dept. of Transportation, Federal Aviation Administration; 2020.

[25] Park C-K, Queitzsch G, Carney K, Du Bois P, Kan C-D, Cordasco D, Emmerling W. *Ballistic Impact Simulations of an Aluminum 2024 Panel using *MAT_224 in LS-DYNA Considering Oblique Incidence and Attitude Angles of a Rectangular Projectile*, DOT/FAA/TC-19/41, P3. Washington, DC, USA: U.S. Dept. of Transportation, Federal Aviation Administration; 2020.

[26] Seidt JD, Gilat A. Plastic deformation of 2024-T351 aluminum plate over a wide range of loading conditions. International Journal of Solids and Structures 2013; 50:1781–90. https://doi.org/10.1016/j.ijsolstr.2013.02.006.

[27] Seidt JD. Development of a New Metal Material Model In LS-DYNA® Part 3: Plastic Deformation and Ductile Fracture of 2024 Aluminum Under Various Loading Conditions. Washington, DC, USA: U.S. Dept. of Transportation, Federal Aviation Administration; 2014. DOT/FAA/TC-13/25, P3.

[28] Pereira JM, Revilock DM, Lerch BA, Ruggeri CR. Impact Testing of Aluminum 2024 and Titanium 6Al-4V for Material Model Development. Washington, DC, USA: U.S. Dept. of Transportation, Federal Aviation Administration; 2013. NASA/TM—2013-217869 and DOT/FAA/TC–12/58.

[29] Ruggeri CR, Revilock DM, Pereira JM, Emmerling W, Queitzsch Jr GK. Impact and Penetration of Thin Aluminum 2024 Flat Panels at Oblique Angles of Incidence. Washington, DC, USA: U.S. Dept. of Transportation, Federal Aviation Administration; 2015. NASA/TM—2015-218484 and DOT/FAA/TC-15/7.

[30] National Institute for Aviation Research, *AL-2024-T3 Test Report*, 2019-02-28_Al2024-T3_Results_Summary.pdf, 2019. Wichita, USA: National Institute for Aviation Research.

[31] Livermore Software Technology Corporation (LSTC. LS-DYNA Keyword User's Manual. Livermore, USA: Livermore Software Technology Corporation; 2019.

[32] Li Y, Ren X, Zhao T, Xiao D, Liu K, Fang D. Dynamic response of stiffened plate under internal blast: Experimental and numerical investigation. Marine Structures 2021;77:102957. https://doi.org/10.1016/j.marstruc.2021.102957.

[33] Dobratz B, Crawford PC. Lawrence Livermore National Laboratory Explosives Handbook: Properties of Chemical Explosives and Explosive Simulants. Springfield, USA: National Technical Information Service, US Department of Commerce; 1985. Report no. UCRL52997 Change 2.

[34] LS-DYNA Aerospace Working Group. Modeling Guidelines Document Version 21-1. Livermore, CA: ANSYS-LST; 2022. awg.lstc.com/tiki-index.php?page=Resources, retrieved 1-27-.